Flexible nanocarbon electrodes for holistically engineered solar cell and battery integrated piezoresistive sensor

Brindha Ramasubramanian[1,2,3], Vundrala Sumedha Reddy[1], Zhen Ye[1], Wei Peng Goh[3], Le Yang[3], Seeram Ramakrishna[1*], and Vijila Chellappan[2,3*]

[*1]Center for Nanotechnology and Sustainability, Department of Mechanical Engineering, National University of Singapore, Singapore 117574, Singapore

[*2]Institute for Functional Intelligent Materials, National University of Singapore, Singapore, 117544, Singapore

[*3]Institute of Materials Research and Engineering (IMRE), Agency for Science, Technology and Research (A*STAR), #08-03, 2 Fusionopolis Way, Innovis, Singapore 138634, Singapore

Corresponding author: c.vijila@nus.edu.sg ; seeram@nus.edu.sg

Abstract

Recently, the research spotlight has been drawn to carbon nanomaterials in the fields of energy, environment, and sustainability. Here, we have developed a sustainable graphitic carbon derived from waste polystyrene plastics (PS-G) and provide a proof of concept for the integration of organic solar cells, Al-ion batteries, and piezoresistive sensors based on PS-G electrodes. Firstly, a flexible organic solar cell (OSC) with the PS-G interfacial layer between the photoactive material and Al metal has enhanced charge extraction mobility with power conversion efficiency (PCE) of 3.5%. A new range of possibilities in metal:semiconductor:carbon:metal contact and interfacial tuning in OSCs are made possible by the fact that pure PS-G without Al can successfully extract electrons with a PCE of 0.89%. Secondly, when used as the cathode in an Al-carbon battery, PS-G demonstrated a specific capacity of 148 mAh g^{-1} at 50 mA g^{-1}. At different current densities, PS-G cathodes demonstrated high cycling stability (with 65% capacity retention over 100 cycles). The performance has deteriorated over cycles due to the presence of oxygenated functional groups over the electrode surfaces. Finally, the best of the fabricated OSCs and Al-carbon batteries were then combined with a piezoresistive sensor that included an active PS-G electrode. Due to the interruption of the electron conductive path and C=C bond breakage, the battery-powered sensor had a resistance of 40 to 45 x10^4 Ω while the solar-powered sensor had a resistance of 32 to 35 x10^4 Ω, when subjected to mechanical stimuli, with a tensile strength of 20 N. This work provides a new opportunity for the design of wearable, self-powered, sustainable electronic devices and to potentially advance the development of PS-G integrated device technologies.

Keywords: Organic solar cell, Graphitized Carbon, Al-carbon battery, Sustainability

1. Introduction

The global population growth and expanding economy have resulted in an annual increase in energy demand (418 EJ).[1] Fossil fuels are primarily used to provide the world's energy needs.[1] Concerns about atmospheric pollutants such as SOx and NOx emissions, along with the depletion of fossil fuels, have recently arisen in several parts of the world. Consequently, there is a growing demand for sustainability in light of various environmental issues and continuously changing climatic conditions. Extensive research has been conducted in recent decades to develop sustainable gadget technology.[1] This insight focuses on the benefits that materials-based solutions can provide, demonstrating how the design and enhancement of sustainable material characteristics can lead to optimized integrated electronic devices that are on par with current wearable technologies.[2] Most wearable flexible pressure sensing systems on the market today require an external power source in the form of a battery. This requirement restricts the development of smart electronic gadgets due to their bulky form factor, making them cumbersome.[2]

Researchers have primarily focused on enhancing the design and composition of sensor systems to address the aforementioned issues. They have also integrated multifunctional equipment to realize self-powered sensing systems.[2] However, the development of multidevice integration systems based on sustainable materials is highly challenging. Building sensors with excellent sensing performance and self-powered capability is a significant problem. It is extremely difficult to create wearable sensors that combine high sensitivity and performance with sustainable self-powering and storage capabilities.[2]

To address the aforementioned issues, we propose utilizing porous carbon nanostructures recovered from recycled plastics for various applications: (i) as a buffer layer for the top electrode in an organic solar cell, (ii) as a cathode in an Al-carbon battery, and (iii)

as an electrode for a piezoresistive wearable sensor. Furthermore, we integrated these devices as solar-powered and battery-powered sensors, highlighting the future research direction for next-generation smart gadgets.

1.1 Selection of sustainable materials and device technologies

Plastic trash production increases because of increased plastic usage. In 2020, almost 367 million metric tons were produced globally.[3] Plastic trash is known to be a contributing factor to global warming and hence, the advancement of recycling methods for plastic waste is becoming crucial.[3] Worldwide, thermal and mechanical recycling techniques dominate, but chemical recycling is mainly limited to a small number of nations, like Japan.[4] Because the generated hydrocarbons may be used as fuel or feedstock to develop new materials, chemical recycling is considered an ecologically acceptable process.[3] We utilized an eco-friendly fluidized bed reactor to synthesize carbon, specifically PS-G, PE-G, and PET-G, derived from three different plastics: polystyrene, polyethylene, and polyethylene terephthalate, respectively.[5] The hydrophobic characteristic of the synthesized graphitic carbon was altered to be hydrophilic through multiple acid treatments and subsequently used as electrodes in three different devices. Finally, the solar and battery components were separately integrated with the piezoresistive sensor as power sources. The Pmax of the solar cell is 0.8 V, while the battery has a voltage rating of 1.9 V. Below, we describe the background for device selection and the state-of-the-art design for all three devices.

Device #1 (Energy Harvester): The advantages of lightweight, inherent flexibility, and sustainability make organic solar cells (OSCs) one of the most attractive clean energy alternatives. Recently, allotropes of carbon have been used as a support layer for matching the gap between the highest occupied molecular orbital (HOMO) and lowest unoccupied molecular orbital (LUMO) of photoactive polymers, and as a buffer layer for top electrodes to collect

electrons effectively.[6] Most importantly, OSCs can be efficiently integrated with batteries as they are flexible and slim. Interestingly, OSCs had a global market of around $55 million in 2019 and is expected to reach about $100 million in 2027.[7] Thus, OSCs are one of the appealing potentials technologies in the near future for powering flexible and transparent smart gadgets. The state-of-the-art flexible OSCs has a power conversion efficiency (PCE) of 16 to 19% for the device area of 1 to 206 cm^2.[7–10] Higher sheet resistance in flexible transparent electrodes (FTEs) underscores the necessity for advancements in large-area FTE technologies to enhance the performance of flexible OSCs. [9,10] The active layers in OSCs are mostly biodegradable polymers. However, the electrodes, made of ITO and metal for hole and electron collection, are non-biodegradable. Further, the fabrication of the top metal electrode using thermal beam evaporation is considerably expensive. Instead, the improvement of Device #1 OSCs is focused on employing a biodegradable carbon recovered from recycled plastics as a buffer layer for metal electrode and then using it as a top electrode by understanding the charge transport.

Device #2 (Energy Storage): The market for Li-ion batteries is constrained by the scarcity and cost of Li metal. From 2022 to 2031, Al-ion batteries (AIBs) are anticipated to expand at a compound annual growth rate (CAGR) of 6.6% globally, worth US$ 4.2 Bn by 2031.[11] An AIB is still in its infancy and the performance is predicted to increase considerably in the following years. Since Al-based batteries are superfast rechargeable batteries, they represent an upgrade over conventional batteries. Due to its low cost, quick charging capability, nonflammability, high charge capacities with metallic aluminum anodes based on three-electron redox characteristics, and a theoretical energy density of 8042 mAh g^{-1}, Al-based batteries are considered essential for the future, offering enhanced safety due to aluminium's low reactivity with electrolytes, thereby reducing flammability risks compared to traditional lithium-ion batteries (LIBs).[12]

A concern for this developing market is that AIBs have a shorter shelf life compared to other alternatives and fewer market participants, contributing to their relative immaturity compared to LIBs. The state-of-the-art Al-carbon battery exhibits a specific capacity of approximately 150 to 300 mAh g^{-1} at a current density of about 30 mA g^{-1}.[13] We used porous carbon recovered from plastics as a cathode, highlighting the potential of sustainable electrodes for the next generation of Al-ion batteries. Fortunately, aqueous AIBs with solid electrolytes are one of the potential sustainable electrochemical energy storage technologies. In addition to better electrochemical performance, these fabricated AIBs offer high safety, low production costs, less pollution, and increased load-bearing capabilities.[12]

Device #3 (Piezoresistive sensor): Among the most demanding sensors, a piezoresistive sensor may be utilized in wearable applications. This includes smart textiles, continuous health monitoring based on piezoresistive sensors that are sturdy, effective, lightweight, and sustainable have so far been developed by researchers. Perovskite ceramic substance (lead zirconate titanate, or PZT), utilized most frequently in manufacturing piezoresistive sensors, serves as the sensing component.[14] However, concerns about the high cost, complicated production methods, and toxicity of perovskites must be addressed. In contrast, carbon is inexpensive, readily available, and suitable for use in piezoresistive sensors. Thus, we utilized carbon to measure its piezoresistive sensing activity, powered by solar and battery sources. Recently, polymers such as polyvinylidene fluoride (PVDF), polydimethylsiloxane (PDMS), and poly(lactic-co-glycolic acid) (PLGA) composites have been employed in piezoresistive sensors. Additionally, carbon and its 2D composite thin films have also been used. [14] However, thin layer piezoresistive sensors, when used in real-world applications, exhibit small effective volumes, and their modest piezoresistive outputs are unable to achieve great responsiveness. For low dimensional structures like nanosheets, the piezoresistive current and voltage outputs are just a few hundreds of mV and pA, respectively.[14] This limitation arises

because the current conducting paths in these structures have weak mechanical stability and break under tensile load, preventing long-term durability. Interruptions in the current conducting path due to mechanical instability can cause electrical discontinuities, increased resistance, or complete electrical failure. Therefore, mechanical stability and piezoresistive sensitivity are crucial when designing flexible sensors.

1.2 Sustainable flexible electrodes for integrated devices

Herein, we report plastic derived graphitic carbon as a sustainable electrode for flexible OSC, Indium Tin Oxide on Polyethylene Naphthalate/Poly(3,4-ethylenedioxythiophene) (styrenesulfonate)/Poly[[4,8-bis[(2-ethylhexyl)oxy]benzo[1,2-b:4,5-b']dithiophene-2,6-diyl][3-fluoro-2-[(2-ethylhexyl)carbonyl]thieno[3,4-b]thiophenediyl]] acid methyl ester/PS-G (ITO:PEN/PEDOT:PSS/PBDTTPD:$PC_{70}BM$/PS-G), the detailed fabrication steps can be found in **Experimental section.** In total, 9 different device combinations were attempted by varying the active material, and the cathode. Three different donors:acceptor bulk heterojunction combinations were used: (i) P3HT:$PC_{60}BM$ (ii) DPPDTT:$PC_{70}BM$ (iii) PBDTTPD:$PC_{70}BM$. Among these, PBDTTPD:$PC_{70}BM$ exhibited the highest charge mobility (10^{-6} to 10^{-3} cm^2 $V^{-1}s^{-1}$ at 7.3 x 10^4 to 1.0 x 10^4 V/cm) with PCE of 3.5%. The charge mobility with varying electric field was studied using photo Charge Extraction by Linearly Increasing Voltage (photo-CELIV) measurements. Furthermore, for the first time, instead of collecting electrons using a top metal electrode, we employed sustainable PS-G (without any metal). Secondly, coupling the reduced wettability of graphitic carbon with the chemical, mechanical stability assisted in the exploration of alternative cathode materials for aqueous Al-batteries. We used the as-synthesised graphitic carbon with PVDF binder coated on carbon cloth as cathode and Al treated in $AlCl_3$-[EMIm]Cl as anode and aluminum trifluoromethanesulfonate, $Al(OTF)_3$ as the electrolyte. The Al-carbon battery maintained a consistent capacity of 148 mAh g^{-1} at a current density of 50 mA g^{-1}. Additionally, under these conditions, the PS-G

cathodes exhibited cycling stability at varying current densities, with 65% capacity retention over 100 cycles.[15] The consistent coulombic efficiencies, ranging from 90% to 100% regardless of the current density applied, demonstrated optimal electrochemical properties. Furthermore, the battery can discharge and charge rapidly at different rates without losing structural integrity. Thirdly, we fabricated a stress/strain sensor by depositing PS-G on carbon cloth, with Al and Cu contacts, and tested its sensing behavior under mechanical stress. We then individually integrated the solar cell and Al-carbon battery with the piezoresistive sensor to demonstrate real-time human motion sensing. This setup allows for the conversion of human body stimuli into electrical signals by altering the battery's internal resistance through mechanical stress. This study presents a novel concept for the development of self-powered sensors. **Scheme 1** provides an overview of the device design.

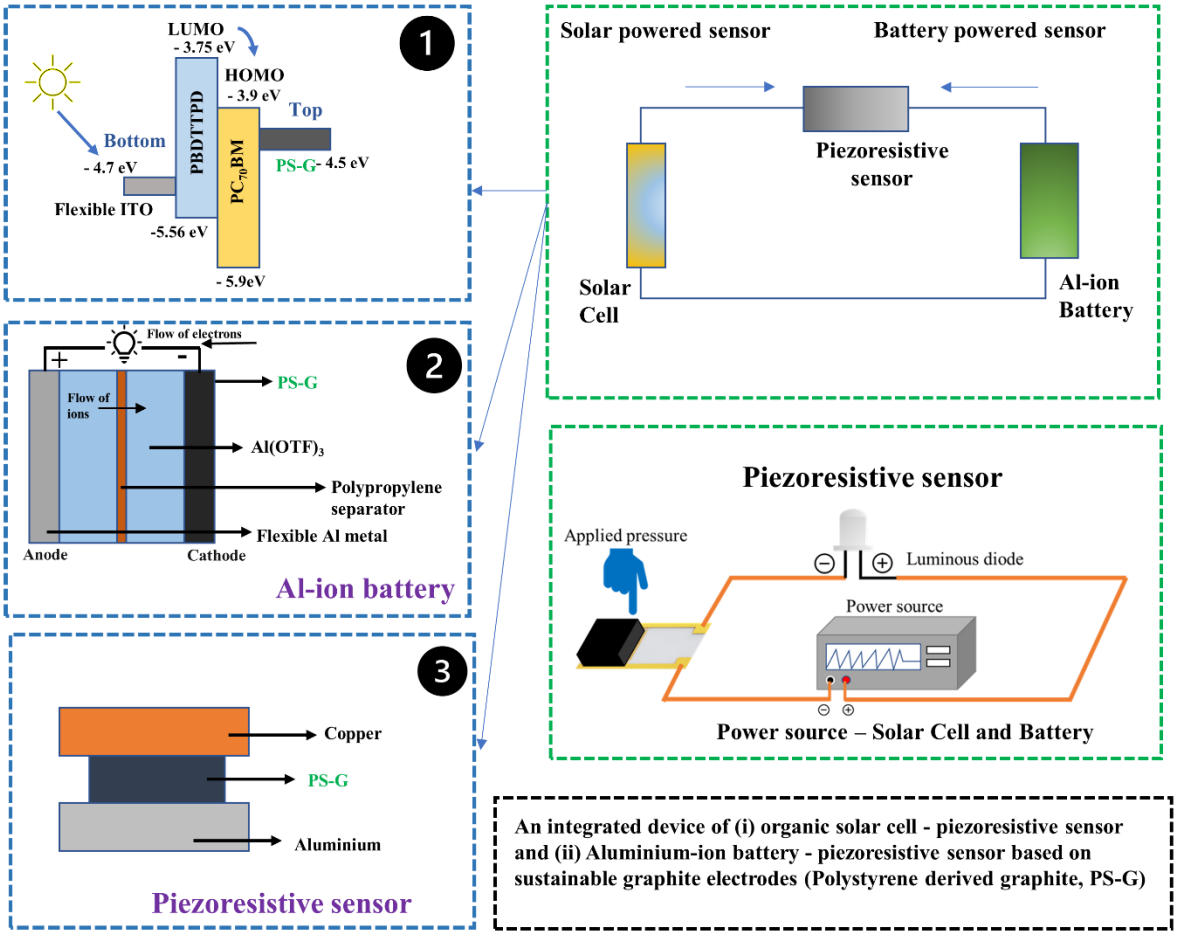

Scheme 1. Illustration of device assembly of (1) flexible OSC, (2) Al-ion battery, (3) piezoresistive sensor into a working device.

2. Results and Discussion

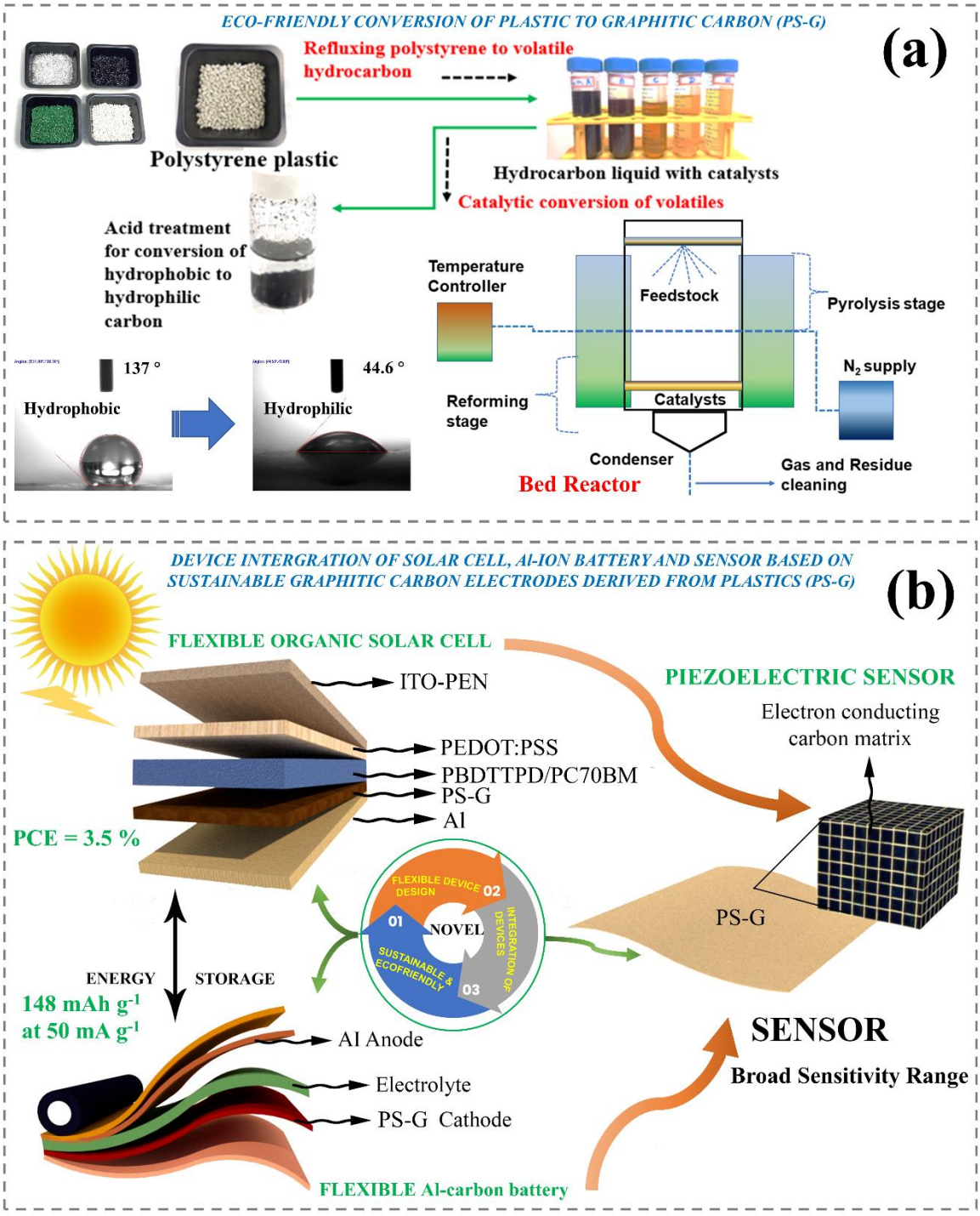

Fig. 1 (a) Schematic illustration of conversion of recycled plastic wastes into graphitic nanocarbon with contact angle measurements for conversion of hydrophobic to hydrophilic PS-G (b) Schematic illustration of device architecture for the fabricated OSC, Al-carbon battery and piezoresistive sensor.

The Experimental section goes into detail about the PS-G electrode's active material's synthesis procedure. In essence, as shown in **Fig. 1a**, recycled plastics were converted into graphitic carbon (G) using thermal treatment and catalytic conversion process.[5] Polyethylene, polystyrene, and polypropylene were heated separately in a sealed furnace in a fluidized bed reactor at 700°C for 2 hours. Cooler coils were used to condense the volatile gas into a liquid, which was later used as feedstock for combustion. The black residues from the furnace were collected and treated with 1 M HCl and DI water several times, followed by centrifugation at 10000 rpm for 20 min and ball milled at 1:20 (sample: ball [2 mm dia]) ratio at 8000 rpm for 2 hours to form graphitic carbon nanoflakes (PS-G, PE-G and PET-G). PS-G has a high carbon content (Table supplementary) with lesser impurity (<0.1%), which was used for all device testing. The produced graphitic carbon had hydrophobic characteristics, making it incompatible for integrating into aqueous Al batteries. Hence, it was rendered hydrophilic via surface functionalization using H_2SO_4 and HNO_3. The contact angle measurement was taken to confirm the hydrophobicity (137°) to hydrophilicity (44.6°) transition as shown in **Fig. 1a**. Overall, the best device configurations are shown in **Fig. 1b**, In OSCs, PBDTTTPD:PC70BM bulk heterojunction with PS-G buffer layer supporting Al top electrode was the best configuration with PCE of 3.5%. For Al-carbon battery, chemically treated Al anode, aqueous $Al(OTF)_3$ electrolyte and PS-G coated carbon cloth had a specific capacity of 148 mAh g^{-1} at 50 mA g^{-1}. Another important characteristic of the graphitic carbon is that it remains suspended in aqueous $Al(OTF)_3$ electrolyte, proving its stability without getting dissolved in the electrolyte which is shown in the **Supplementary video file S-1**.[16] . Layered carbons do not experience the dramatic structural collapses or rearrangements and are conductive, in addition to being flexible hosts for electron trapping. These features enable carbon to be an attractive candidate as a top electrode in OSCs. For optimization, three different

donor:acceptor combinations were investigated. Metallic Al, commercial graphene quantum dots and PS-G as top electrodes were used and compared, similar to [17]

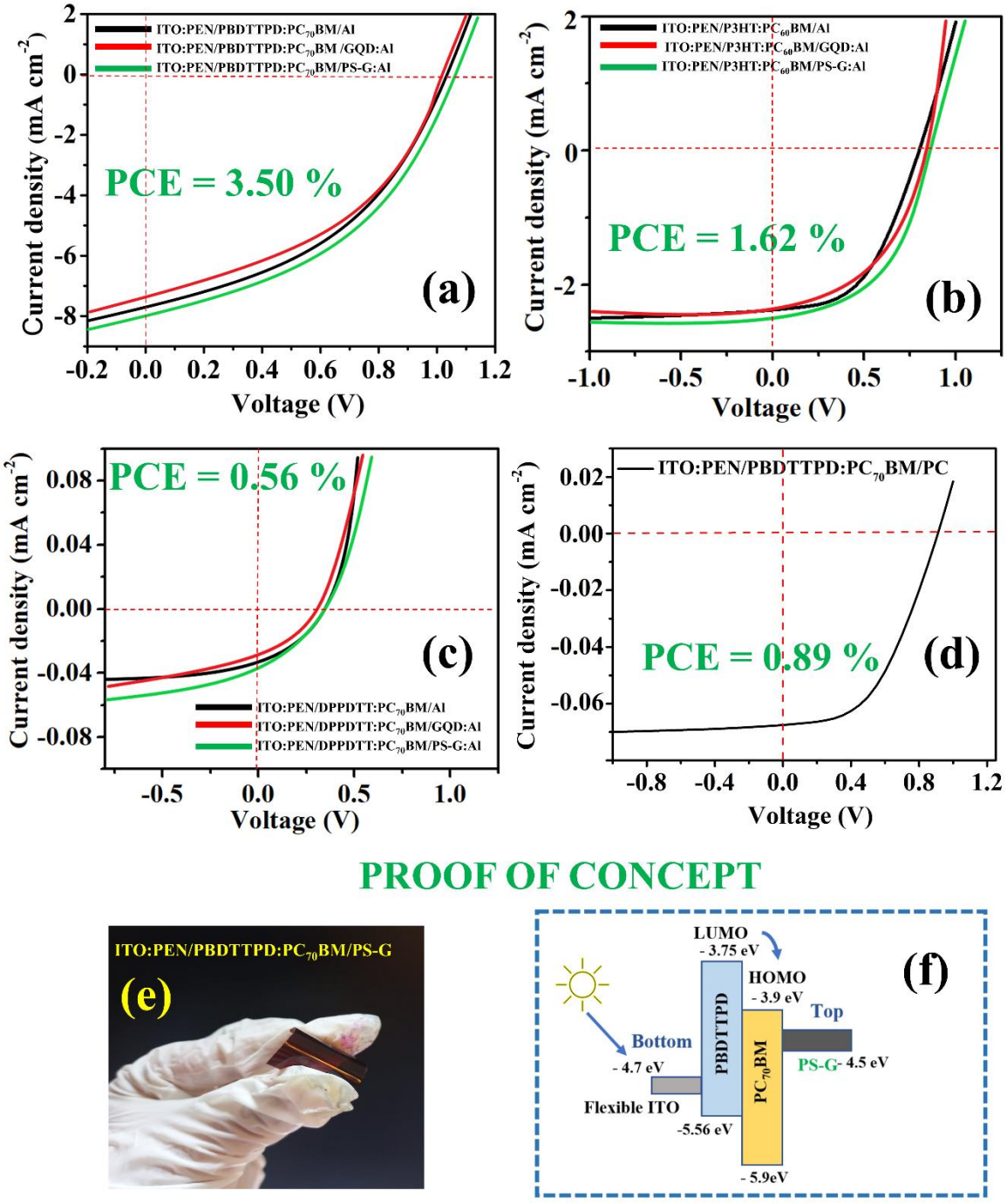

Fig. 2 (a) I–V characteristics of the flexible OSCs with PBDTTPD:$PC_{70}BM$ in different device structures with Al, GQDs-Al, and PS-G:Al as top electrodes; (b) I–V characteristics of the flexible OSCs with P3HT:$PC_{60}BM$ in different device structures with Al, GQDs-Al, and PS-

G:Al as top electrodes; (c) I–V characteristics of the flexible OSCs with DPPDTT:$PC_{70}BM$ in different device structures with Al, GQDs-Al, and PS-G:Al as top electrodes; (d) I–V characteristics of the flexible OSCs optimized with PBDTTPD:$PC_{70}BM$ and PS-G as top electrode ; (e) photograph of the fabricated flexible OSC; (f) energy band diagram for the PS-G top electrode configuration with PBDTTPD:$PC_{70}BM$ as active layer.

In high performance flexible OSCs, the electrode buffer layer between the electrode and the active layer plays a critical role. The interface layer can both provide impedance match, ohmic contact between the active layer and electrodes, and improve charge extraction.[18] Here, PS-G was used as an electrode buffer layer in one device configuration and as a top electrode in another configuration. **Fig. 2a** shows the I-V characteristics of the devices ITO:PEN/PBDTTPD:$PC_{70}BM$/Al, ITO:PEN/PBDTTPD:$PC_{70}BM$/GQD:Al (Commercially available graphene quantum dots) and ITO:PEN/PBDTTPD:$PC_{70}BM$/PS-G:Al (synthesised carbon) under simulated AM1.5G, 1000 W/m^2, with PCEs of 3.28%, 3.41%, 3.50% respectively. [19] The device with PS-G:Al as the top electrode produced the highest short circuit density as compared to those with Al and GQDs:Al as the top electrode. The high conductivity from PS-G and the efficient energy level alignment may be responsible for the enhanced photocurrent's mechanism.[19] It is clear that the alignment of energy levels has accelerated the charge transport while simultaneously suppressing recombination of charges.[20] The conductivity of PS-G has improved the extraction of electrons from the donor: acceptor layer. All these processes take place in the presence of the built-in field alone, i.e., no additional voltage was applied. The layered graphitic structure and nanoscale properties are crucial for obtaining the photovoltaic effect; any flaws might serve as recombination traps and reduce the photovoltaic effect.[21,22] The amount of charge collected also affects how much photocurrent the device produces. Thus, the nanocarbon and layered structures provide a favorable photovoltaic effect.[19] Smith et al. recently studied the interfacial kinetics and

charge transport in PBDTTPD:$PC_{70}BM$ bulk heterojunction OSC. The PBDTTPD polymer with linear chains and combination of linear-branched chain had different PCEs of 4 and 8% respectively.[23] Despite the fact that side chain changes had no effect on the exciton disintegration and ultrafast charge production processes, Smith et al. and group have proved that polymers with branches show a lowered rate of recombination and a smaller proportion of sub-nanosecond recombination.[23] Short circuit rates had therefore increased by 33% as the yield of long-lived carriers increases. The structure, property and individual charge transport studies of the polymers used such as P3HT, $PC_{70}BM$, $PC_{60}BM$, DPPDTT and PBDTTPD were reported previously in literatures.[21] The energy level diagrams and the device structure for all nine devices are shown in **Fig. S-3, S-4**. The HOMO:LUMO energy levels of PBDTTPD:$PC_{71}BM$ align closer with PS-G, which has aided in the charge transport, thus, minimizing the recombination process.

Similar trends were noted in devices using P3HT:$PC_{60}BM$ and DPPDTT:$PC_{70}BM$, with Al, GQD:Al and PS-G:Al as the top electrode, as shown in **Fig. 2b-c**. The device configurations used for obtaining the I-V curves in **Fig. 2b** are ITO:PEN/P3HT:$PC_{60}BM$/Al (reference), ITO:PEN/P3HT:$PC_{60}BM$/GQD:Al (commercially available carbon) and ITO:PEN/P3HT:$PC_{60}BM$/PS-G:Al (synthesised carbon), with PCEs of 1.18%, 1.48% and 1.62% respectively

The device configurations used for obtaining the I-V curves in **Fig. 2c** are ITO:PEN/DPPDTT:$PC_{70}BM$/Al (standard), ITO:PEN/DPPDTT:$PC_{70}BM$/GQD:Al (commercially available GQDs) and ITO:PEN/DPPDTT:$PC_{70}BM$/PS-G:Al (synthesised carbon), with PCEs of 0.46%, 0.52% and 0.56% respectively. **Fig. 2d** shows the I-V curve of the best performing device utilising PBDTTPD:$PC_{70}BM$ as the active layer and PS-G as the top electrode . The measured short circuit density (J_{sc}) and open circuit voltage (V_{OC}) is 1.104 mA cm^{-2} and 0.287 V, respectively. The value of J_{max} and V_{max} obtained from the graph

is 0.02 mA/cm^{-2} and 0.9 V, respectively. The fill factor (FF) is 0.21. This results in a PCE of 0.89%. **Fig. 2e** shows the fabricated device (based on PBDTTPD:$PC_{70}BM$ as the active layer and PS-G as the top electrode) while Fig. 2f exhibits the energy level diagram. The HOMO:LUMO gap and energy levels of PS-G are closer for the PBDTTPD:$PC_{70}BM$ blend when compared with other two polymer blends allowing the faster transition of charges, as shown in **S-3**. The PCE of the state-of-the-art flexible OSCs is ~18%[8,10], In our study, we obtained a PCE of 3.5% for ITO:PEN/DPPDTT:$PC_{70}BM$/PS-G:Al to assess the feasibility of using recycled plastic-derived carbon as an interfacial layer. Additionally, we obtained a PCE of 0.89% for ITO/DPPDTT/PS-G without aluminum as the top electrode.

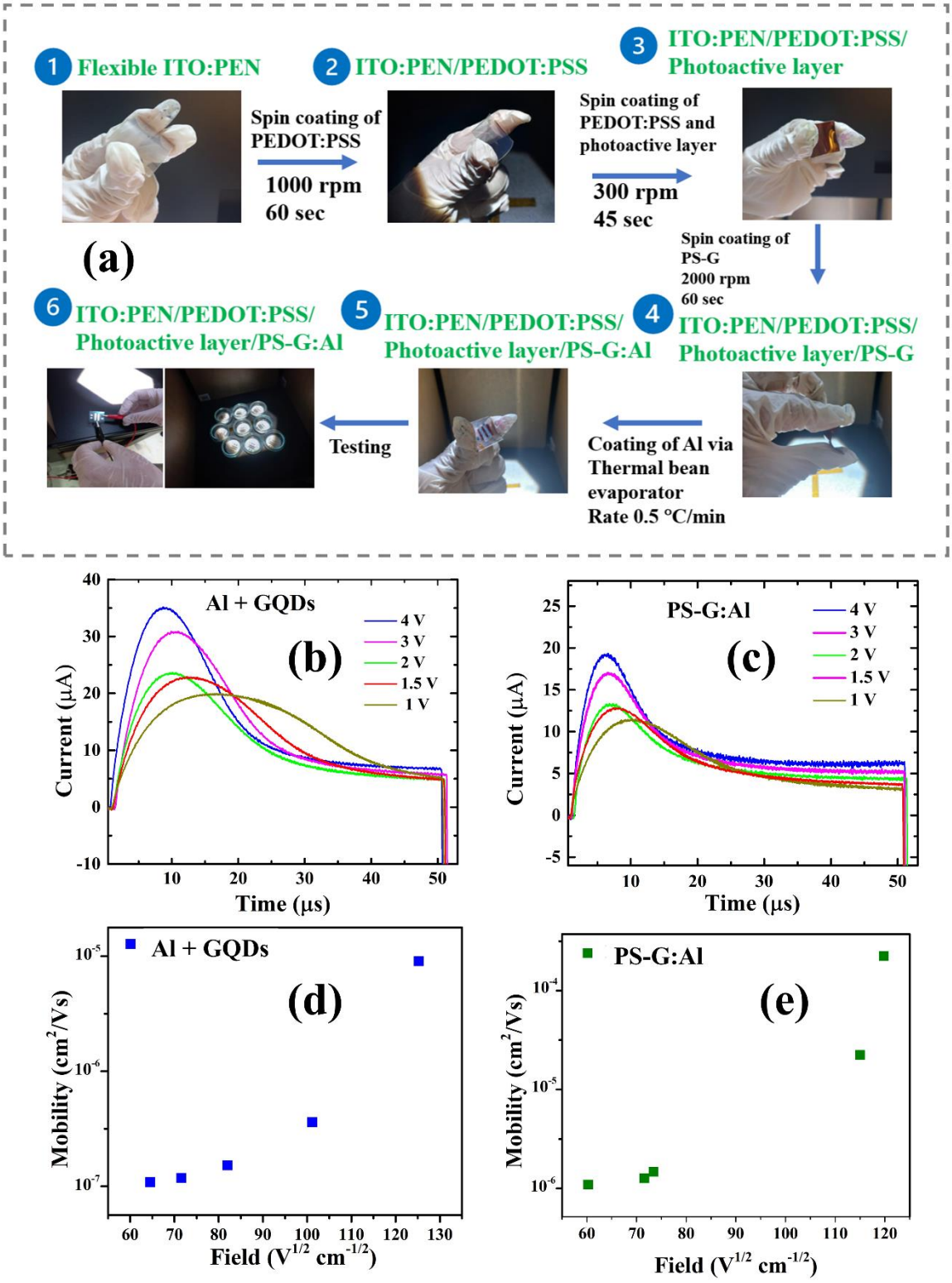

Fig. 3 (a) Schematic overview of the process and parameters involved in the fabrication of flexible OSCs; (b) PhotoCELIV transients for ITO:PEN/PBDTTPD:PC70BM/GQD:Al

device; (c) PhotoCELIV transients for ITO:PEN/PBDTTPD:PC70BM/PS-G:Al device; (d) Variation in charge mobility upon an applied electric field for ITO:PEN/PBDTTPD:PC70BM/GQD:Al device (e) Variation in charge mobility upon an applied electric field for ITO:PEN/PBDTTPD:PC70BM/PS-G:Al device.

Fig. 3a shows a general overview of the cleaning and fabrication steps of the various device configurations. **Fig. 3b** shows the PhotoCELIV measurement of the device with GQD:Al as the top electrode. The PhotoCELIV transients have a specific single-peak pattern and the transit time increases with an increasing applied electric field. The charge extraction time was less for PS-G:Al (6.85×10^{-12} s) than GQD:Al (6.17×10^{-11} s) **(Fig. 3b-c**) proving the faster charge extraction capabilities of PS-G. The charge mobility was between 10^{-7} to 10^{-5} cm^2 $V^{-1}s^{-1}$ for GQD:Al; 10^{-6} to 10^{-3} cm^2 $V^{-1}s^{-1}$ for PS-G:Al for the field applied between 7.3×10^4 to 1.0×10^4 V/cm. The transient shows that the charges took less time to achieve the extraction current maxima for PS-G:Al, indicating that charge mobility is dependent on the interfacial buffer layer **(Fig. 3d-e)**. The device without carbon interfacial layer had similar traits and have been reported in previous literatures.[23,24]

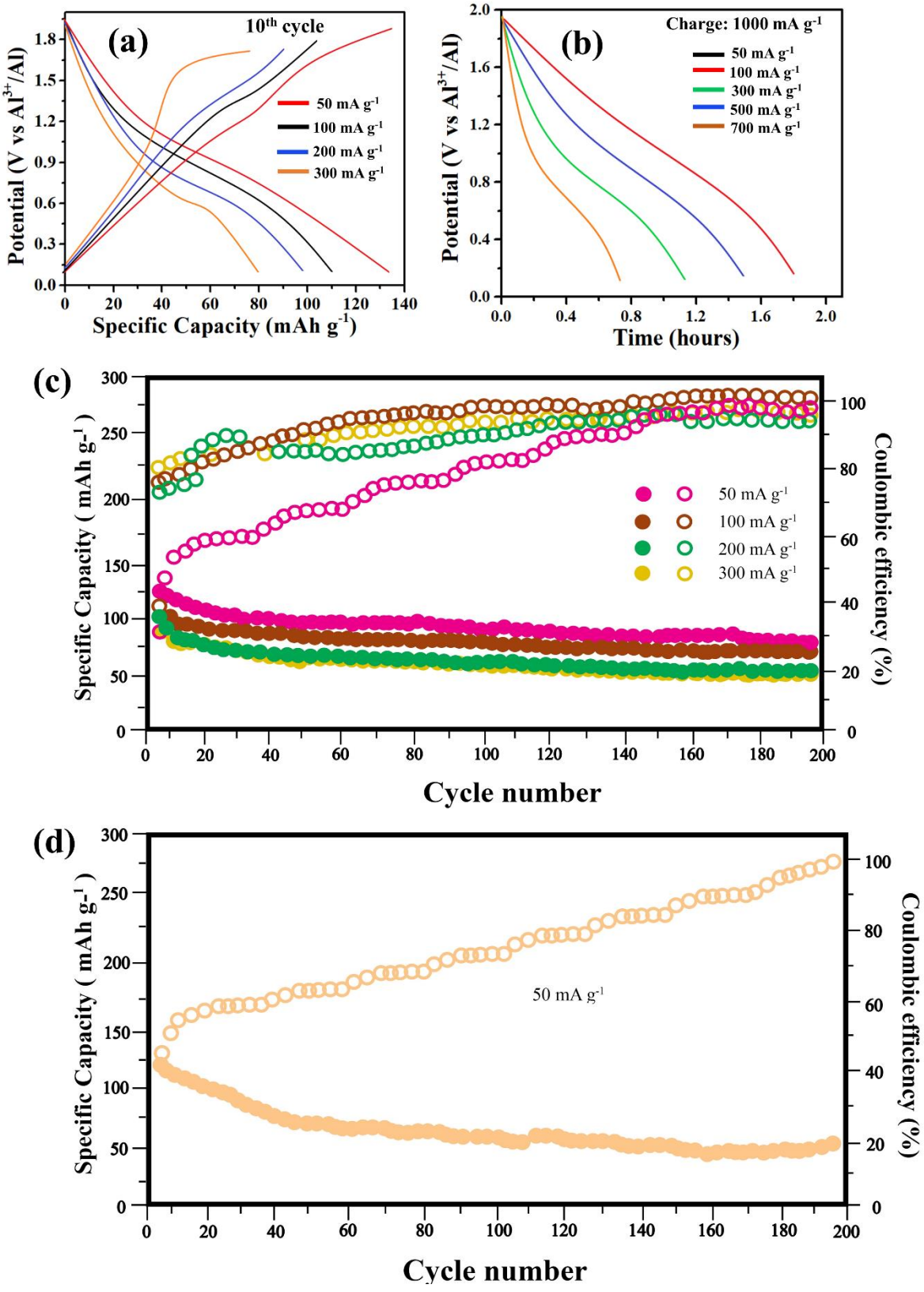
(a)
10th cycle
50 mA g-1
100 mA g-1
200 mA g-1
300 mA g-1
Potential (V vs Al3+/Al)
Specific Capacity (mAh g-1)
(b)
Charge: 1000 mA g-1
50 mA g-1
100 mA g-1
300 mA g-1
500 mA g-1
700 mA g-1
Potential (V vs Al3+/Al)
Time (hours)
(c)
50 mA g-1
100 mA g-1
200 mA g-1
300 mA g-1
Specific Capacity (mAh g-1)
Coulombic efficiency (%)
Cycle number
(d)
50 mA g-1
Specific Capacity (mAh g-1)
Coulombic efficiency (%)
Cycle number

Fig. 4 (a) Potential versus specific capacities of PS-G:Al at various current densities; (b) voltage graph for slow charge and fast discharge; (c) cycling stability of PS-G:Al at different current densities; (d) cycling stability of PS-G:Al at 50 mA g^{-1}.

We observed that electrochemical activity is due to ion insertion into PS-G (intercalation mechanism) based on **Fig. 4**, also the PS-G does not disperse in 3 M $Al(OTF)_3$ electrolyte as shown in **S-1 video**. Thus, this excludes multivalent metal complexes that can generate various oxides during charge/discharge process. For aqueous electrochemical systems, especially those that rely on intercalation processes, it makes sense to utilize electrode materials that interact favourably with water. We initially examined the PS-G wetting behavior using contact angle studies and tested the physiochemical properties of PS-G coated on carbon cloth, as shown in the **Fig. S-5.**

After performing several preliminary experiments with different voltage window (0.1 to 4 V), we decided on the following device parameters: The anode is an Al foil that has been pre-treated with Ionic liquid (IL), the electrolyte is a 3 M $Al(OTF)_3$ solution, and the redox voltage window is 0.1 to 2.0 V. The device sustained a constant capacity of 148 mAh g^{-1} at 50 mA g^{-1} (**Fig. 4a**). Further, the PS-G:Al cathodes in these circumstances demonstrated outstanding cycling stability at various current densities (with 65% capacity retention over 100 cycles).[NO_PRINTED_FORM] The exceptional electrochemical characteristics of the cells are shown by the continuous Coulombic efficiencies in the 90 to 100% independent of the current density used. The galvanostatic charge/discharge profiles at various current densities were examined. The PS-G:Al cells consistently displayed sloping discharge patterns at about 1.88 V (**Fig. 4b**). Such predictable behavior in carbon cathodes often suggests a considerable contribution from pseudocapacitive charge storage.[15] The functional stability of carbon electrodes at high current densities, as shown by Dai et al. for non-aqueous Al-batteries, is a crucial benefit. Our PS-G:Al cell could not sustain functioning for more than fifteen cycles

when pushed to 1000 mA g^{-1} **(Fig. 4b)**. Besides, it had a diminished starting capacity of 28 mAh g^{-1} and showed a 12% decline before breaking down. The performance of the prolonged cycle stability run served as the concluding test of the PS-G:Al cathode's durability (**Fig. 4c-d**). The cell could be used for 200 cycles (at 50 mA g^{-1}) and maintained a steady capacity of > 60 mAh g^{-1} (**Fig. 4d**).[17] Previous literatures have also supported the use of carbon cathodes in AIBs.[17,25]

There is still disagreement on the method of charge storage in aqueous Al-batteries, specifically the species reaction of the intercalant. Layered carbons are less susceptible to severe structural collapses and rearrangements, and irreversible redox changes that may occur in metal oxides, making them adaptable hosts for molecular and ionic species.[15]

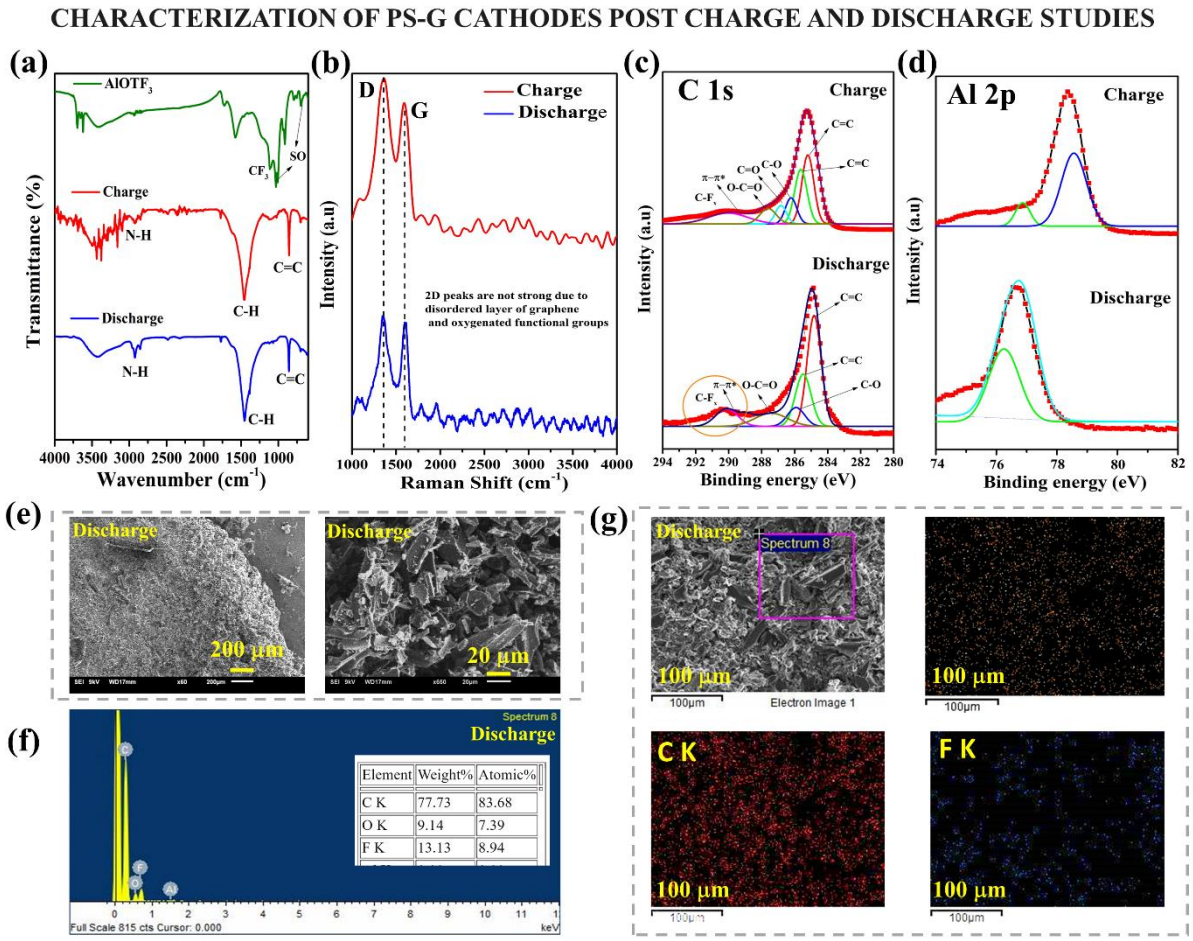

Fig. 5 Post cyclic characterizations of PS-G cathode using (a) FTIR; (b) Raman; (c) C 1s XPS spectra; (d) Al 2p XPS spectra; (e) FESEM ; (f) EDX spectrum and (g) EDX elemental mapping.

Fourier Transform Infrared Spectroscopy (FTIR) studies were done to identify the predominant functional groups in the cycled PS-G (**Fig. 5a**). The electrolyte anion OTF showed a number of peaks, namely those at 1278, 1051, and 675 cm^{-1}. It should be noted that during discharge, the amplitude of the C-O stretching band experiences a 20 cm^{-1} redshift.[26] Given that this band is highly reactive to its organic surroundings, electrical charge transfers might be the cause of the change. This is in line with electron spin resonance study, which shows that Faradaic reactions exist at clusters that include oxygen [20]. Further, the electrolyte is aqueous, which enables higher possibilities of having oxygen containing functional groups in the discharged PS-G. Raman spectra in **Fig. 5b** illustrate how minimally the charged and discharged states differ from each another, along with minimal frequency or broadening of the G-band. Both observations demonstrate the stability of PS-G. The 2D peak was weak due to the disordered graphitic layers, which arose from continuous cycling and the presence of oxygenated functional groups on PS-G.[27] XPS was used to examine the cycled PS-G surface (**Fig. 5c-d**). The C 1s spectra indicated the presence of the C-O, and O-C-O for both charged and discharged conditions, which are centred at 286.2, 287.6, and 288.6 eV, respectively, along with the sp^2 and sp^3 C species. This is similar to earlier reports. [28] It is noteworthy that the CF_3SO_3 anion is the source of the peak at 292.8 eV, which is linked to a C-Fx bond. In Al 2p spectra, the Al^{3+} ionic transition was seen at 75.8 eV emphasising the presence of aluminum-hydroxide species during charge, which is shifted to a lower binding energy of 74.2 eV after discharge, suggesting an increase in oxygenated functional groups.

Fig. 5e shows the Field Emission Scanning Electron Microscopy (FESEM) images of the PS-G electrodes after discharge. The corresponding Energy-Dispersive X-ray (EDX) spectrum in **Fig. 5f** shows the presence of carbon (77.73 wt%), oxygen (9.14 wt%) and fluorine (13.13 wt%). Fluorine is due to the presence of the PVDF binder. **Fig. 5g** additionally confirms the elemental mapping distribution of carbon and fluorine in the PS-G electrode after discharge.

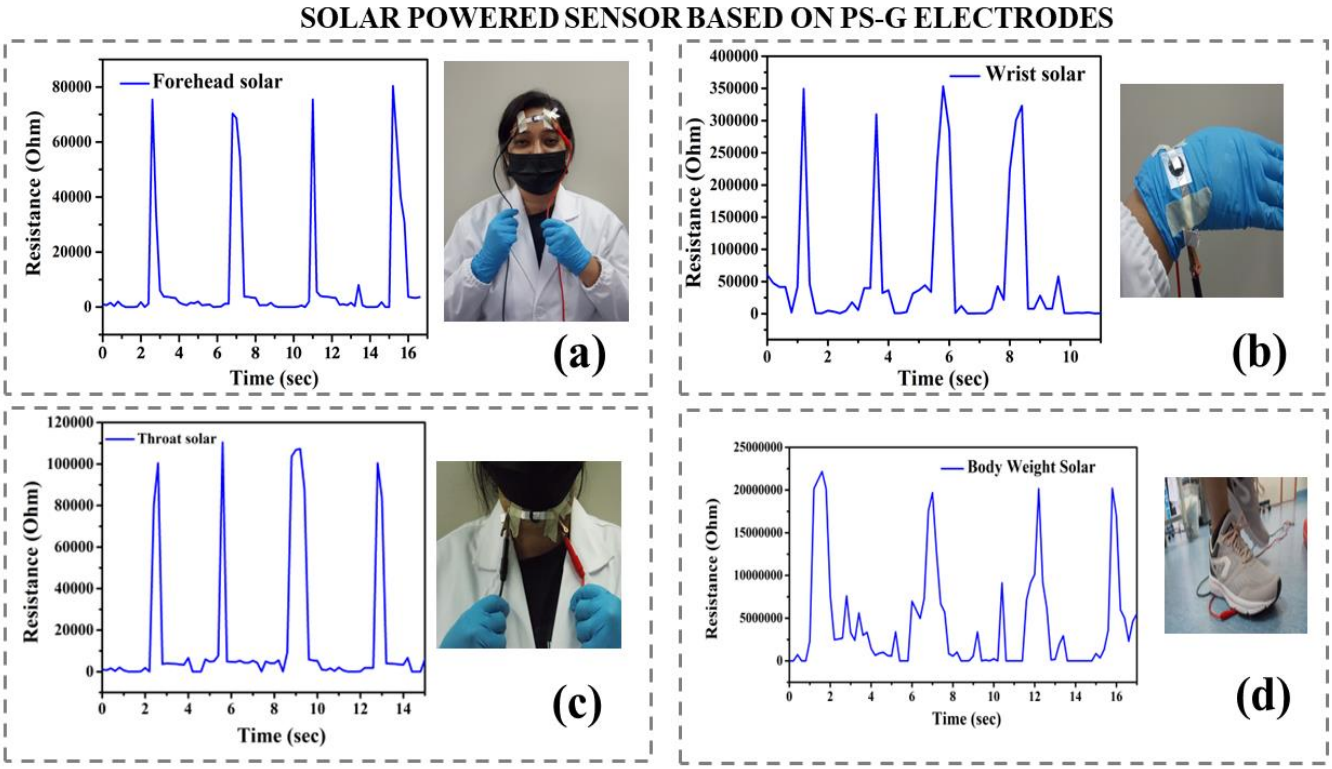

Fig. 6 Variation of resistance with respect to applied mechanical stress powered by 3.5% PCE OSC (ITO:PEN/PBDTTPD:$PC_{70}BM$/PS-G:Al) tested for (a) Forehead; (b) Wrist; (c) Throat (d) Body weight.

The device fabrication of the stress/strain sensor involves introducing synthesized porous carbon paste onto the carbon foam via dip coating which is then allowed to dry in the furnace at 80 ℃ for 12 h. The conductive sample containing non-conductive carbon foam is sandwiched between flexible aluminium electrodes and sealed with a silicone medical tape to provide stability and flexibility. The working principle of the sensor involves application of

physical stress or strain resulting in corresponding reduction in contact points of the PS-G leading to the increased resistance. This resistance change caused by mechanical deformation is the basis of data collection for piezoresistive sensors.[29,30] **Fig. 6a-d** shows the resistance change with respect to applied mechanical stimuli of 20 N. To test the response and the transduction mechanism of our samples, we applied a contact force of 20 N using a tensile compression testing machine. We observed that there was a monotone increase in current with the bias voltage and decrease in current with increasing mechanical stimuli. Hence the higher conductive plastic derived carbon (PS-G) demonstrated higher resistance peaks. Therefore, we conducted piezoresistive testing and measured the resistance outcome with the mechanical stimuli. It was noted that PS-G which had highest conductivity showed higher peaks when compared to PE-G and PET-G samples, which is shown in **Supplementary Information**.

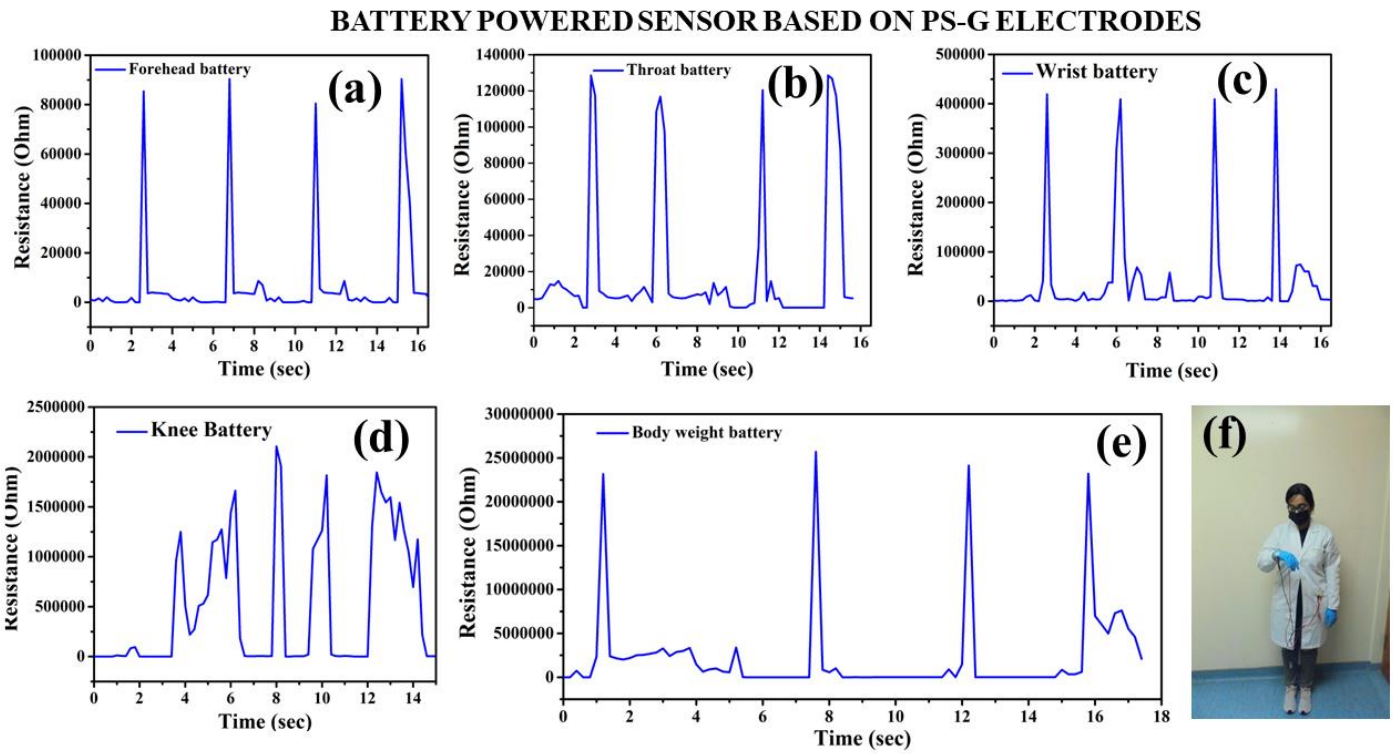

Fig. 7 Variation in resistance with respect to applied mechanical stimuli powered by Al-carbon battery, tested for (a) Forehead; (b) Throat (c) Wrist; (d) Knee; (e) Body weight.

We compared the physiological signal acquisition on different parts of the body with both solar powered and battery powered PS-G sensor. Changes in the resistance due to facial muscles movement could be observed arising from the placement of the sensor (solar or battery powered) at the forehead. The resistance generally increases when muscles contract and decreases when they expand. This is because muscle contraction usually reduces the distance between sensor contacts or compresses the sensor material, leading to higher resistance. A solar powered sensor registered a peak resistance of 7 – 8 x10^4 Ω **(Fig. 6(a))** while a peak resistance of 8 – 10 x10^4 Ω was measured for the battery powered sensor (**Fig. 7(a))**. The sensor was placed on the neck to monitor vibrations from vocalisations. A peak resistance of 10 – 12 x 10^4 Ω was characterised for a solar powered sensor (**Fig. 6(c)); 12** – 13 x 10^4 Ω for a battery powered sensor. A solar powered unit on the wrist produced a resistance peak of 32 – 35 x 10^4 Ω (**Fig. 6(b))** while a resistance peak of 40 – 45 x 10^4 Ω was obtained for a battery powered

sensor (**Fig 7(c))**. Similarly, the sensor unit was attached at the knee joint of leg. The volunteer was holding the leg parallel to ground at 180° and slowly rested the foot on the ground, making the knee bend to 90° at half squat position, this motion can be clearly noticed with the following successive peaks observed in **Fig 7(d)**. Lastly, we utilised the sensor to quantify the body weight of the volunteer **Fig 7(e)**. When someone steps on the sensor, the resistance decreases due to the pressure applied, which compresses the sensor material and reduces the resistance path. Since the body weight exerted higher pressure on the sensor, the resistance values attained a high of 2.6 x 10^7 Ω. The output was comparatively erratic for solar powered unit **Fig 6(d)** when compared to battery powered unit (**Fig 7(e)**) due to higher strain imparted by the volunteer's body weight and the non-homogeneous intensity of ambient lighting. Solar-powered sensors showed lower peak resistances compared to battery-powered sensors in most placements, possibly due to variations in power stability and sensor sensitivity under different power sources. The resistance values varied with the intensity of external stimuli, indicating the sensor's wide working range. The discrepancy in resistance change could also arise from non-uniform pressure application and the dynamic nature of muscle movements.

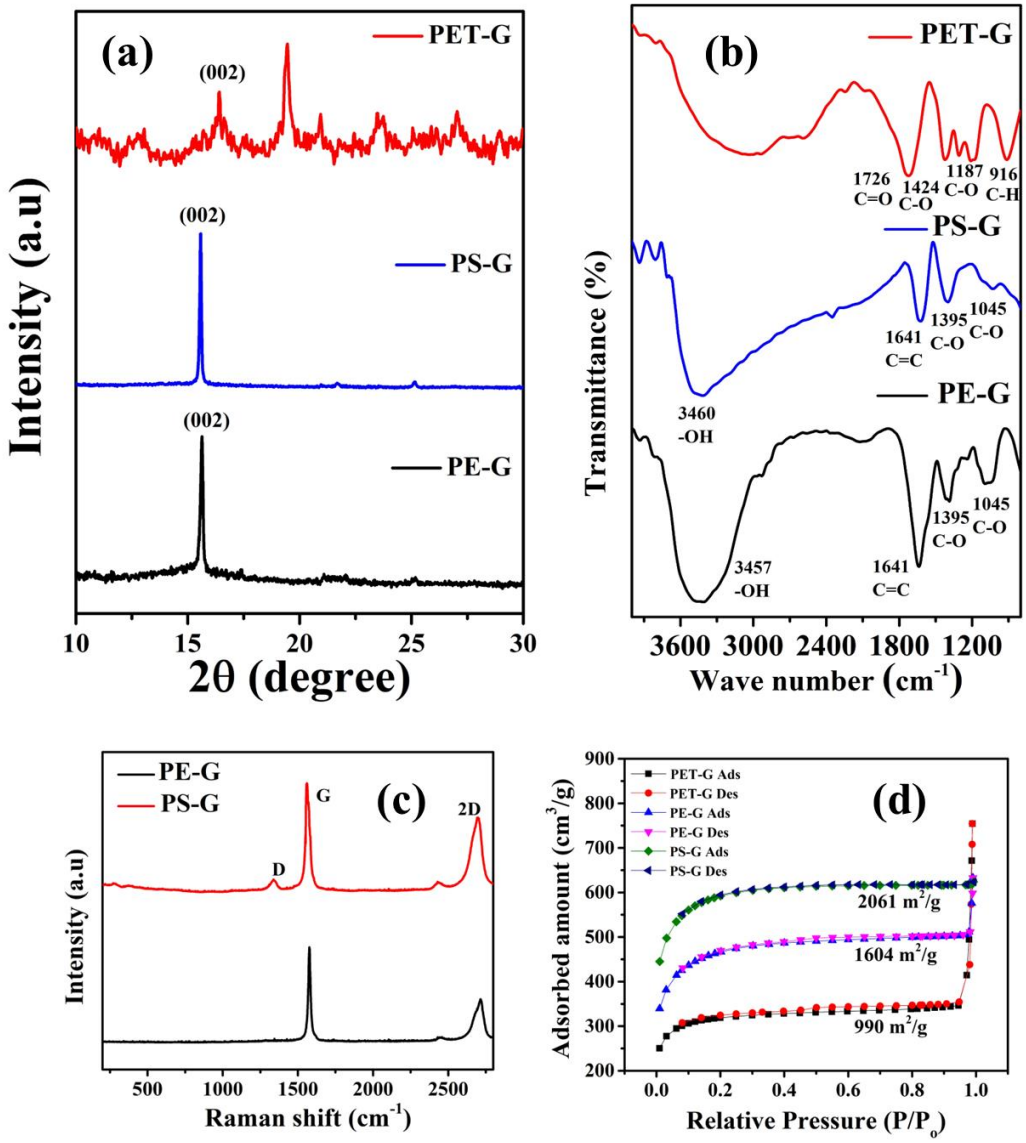

Fig. 8 Material characterization of synthesised PS-G, PE-G and PET-G using (a) XRD; (b) FTIR; (c) Raman; (d) BET surface area.

The X-ray Diffraction (XRD) spectra of PE-G and PS-G as shown in **Fig. 8(a)** have similar diffraction patterns as both PE and PS have ~87% carbon content and have similar polymer chains. Strong peaks at 16.3° corresponding to (002) plane confirms the presence of sp^2 hybridized carbon in the form of graphene oxide, with an interlayer distance of 0.36 nm. In PET-G, the (002) peak has been shifted to 18.7° and has an additional peak at 20.1°. This is analogous to previous reports. [26] This may be due to the impurity and the presence of organic

groups from PET. The FTIR spectra shown in **Fig. 8(b)** confirms the presence of C=C and C-O in all the three samples. Additional C-H stretching band at 916 cm^{-1} has been observed for PET-G. **Fig. 8(c)** shows the Raman spectra with D and G bands at 1348 cm^{-1} and 1589 cm^{-1} respectively. The G band affirms the presence of layered structure with ID/IG ratio of ~1.1. Further, the graphitization degree is low which can be attributed to the peak 2D band at 2655 cm^{-1} and D+G band at 2910 cm^{-1}.[31] Brunauer–Emmett–Teller (BET) nitrogen adsorption plots are shown in **Fig. 8d**. The surface area was incredibly higher for PS-G (2061 m^2/g), followed by PE-G (1604 m^2/g) and PET-G (990 m^2/g).[NO_PRINTED_FORM] It is obvious that the increase in surface area is attributable to the initial plastic source's characteristics and their structural change during carbonization process.

3. Experimental

Preparation of graphitized carbon from plastics

All the chemicals were purchased from Sigma Aldrich Singapore and used without further purification. Recycled polystyrene plastics were commercially purchased from ANR technologies, Singapore. Three plastics, polyethylene, polystyrene, and polypropylene were heat-treated separately in a sealed furnace in a fluidized bed reactor at 700 °C for 2 hours. Cooler coils were used to condense the volatile gas into a liquid, later used as feedstock for combustion. The black residues from the furnace were collected and treated with 1 M HCl and DI water several times, followed by centrifugation at 10000 rpm for 20 min and ball milling at 1:20 (sample: ball ratio, bead size: 2 mm) at 8000 rpm for 2 hours to form graphitic carbon nanoflakes.

Material characterization

The structural characteristics were studied using Bruker D8 X-ray diffractometer with Cu-Kα radiation source at a scan rate of 1 °/min. The morphological and elemental mapping

were carried out using field emission scanning electron microscopy (SEM) SUPRA VP- 4132 Carl Zeiss with EDS (SIGMA-L). Raman spectra was recorded using Ram Spec-HR, 520 nm green laser. The Nicolet iS10 spectrometer was used for measuring the infrared spectrum (FTIR). Brunauer-Emmet-Teller (BET) specific surface area, total pore volume and pore size of the samples are determined by measuring their nitrogen adsorption isotherms at -196ºC using an Automatic High Resolution Physisorption Micropore/ Mesopore Analyzer (ASAP2020MP) System. X-ray photoelectron spectroscopic analysis was performed using Kratos Amicus XPS, with Mg K X-ray source.

Electrochemical characterization and battery fabrication

All the electrochemical studies were carried out in AUTOLAB PGSTAT302N electrochemical workstation and ARBIN, LBT21084 with temperature and humidity controlled by DHTHM-27-20), Shanghai. The Al-carbon 2032 cells were assembled using PS-G and $AlCl_3$:[EMIm]Cl = 1.5 mol mol^{-1} treated Al foil. The PS-G cathodes were prepared in the slurry composition of 80:10:10wt% of active material (PS-G), PVDF binder, acetylene black in N-methyl-2-pyrrolidone (NMP) solvent. The resulting slurry was put into a vial, subjected to sonication for 30 minutes, and thereafter magnetically stirred for 24 hours. The slurry was then spread out on the carbon cloth current collector and allowed to dry overnight at 80 °C in a vacuum. The electrodes were dismantled after charge or discharge cycles operated at 10 mA g^{-1}. The mass loading of active material is 1 mg cm^2. 100 μL of aqueous electrolyte was used for all the experiments.

Solar cell fabrication

The active polymer solution preparations were discussed in the **Supplementary information**. The patterned ITO:PEN was cleaned using detergent, DI water, acetone, and IPA for 30, 10, 15 and 20 minutes, respectively. The cleaned ITO:PEN (1 cm^2) was UV-ozone

treated at 100 °C for 10 min. PEDOT:PSS was then spin coated onto the ITO:PEN substrate at 1000 rpm for 60 s before annealing at 120 °C for 10 min. The active polymer layer was then spin coated at 300 rpm for 45 s inside a N_2 filled glove box., solvent annealed for 2 hours before thermally annealed at 120 °C for 10 min. Then, PS-G or GQD was spin-coated onto the ITO:PEN/PEDOT:PSS/photoactive layer at 2000 rpm for 60 s to form a thin film coating and dried at ambient atmosphere for 2 h. The I-V characteristics of the solar cell was measured using 220/380 V Kewell Power solar simulator and Keithley voltage controller.

Photo Charge Extraction by Linearly Increasing Voltage (PhotoCELIV) was used to measure the charge mobility. A pulse generator (SRS-DG535), a function generator (SRS-DG345), and a digital oscilloscope complemented the PhotoCELIV setup (Agilent, 1 GHz). Laser source with a wavelength of 532 nm was used. The device was subjected to a linearly rising voltage pulse with varying amplitudes, which extracted the equilibrium charge carriers in the device. From the recorded PhotoCELIV transients, estimates were made for the duration (t_{max}), maximum (D_j), and current owing to capacitor displacement (j_0) extraction currents.

Piezoresistive Sensor fabrication

The sensor was fabricated in N_2-filled glove box. 0.5 g of PS-G powder was suspended in 10 mL of ethanol and coated on carbon foam and dried at 80 °C for 3 hours, followed by vacuum heating at 120 °C for 5 hours. The PS-G was then slowly sandwiched between the copper and Al electrodes sealed using transparent medical tapes. Next, the sensor connected to a voltmeter. The voltage was increased in steps of 1 V , from 0 V to 4.5 V. The sensor was placed in different parts of the body and tested for its performance relative to the body motion.

Integration of devices

The solar cell and piezoresistive sensor were connected in series as device 1 (ID-1) and battery and piezoresistive sensor were connected in series, named as device 2 (ID-2). The

device wiring configuration is shown in **Fig. 9**. The whole Al-carbon cell has operating voltage of 1.8 V, capable of powering the sensor. However, OSC has lesser ability to match the efficiency of battery, in terms of specific capacity. The individual devices in ID-1, ID-2 were linked directly. By integrating all components (OSC, battery, piezoresistive) together, a self-powered unit is realised.

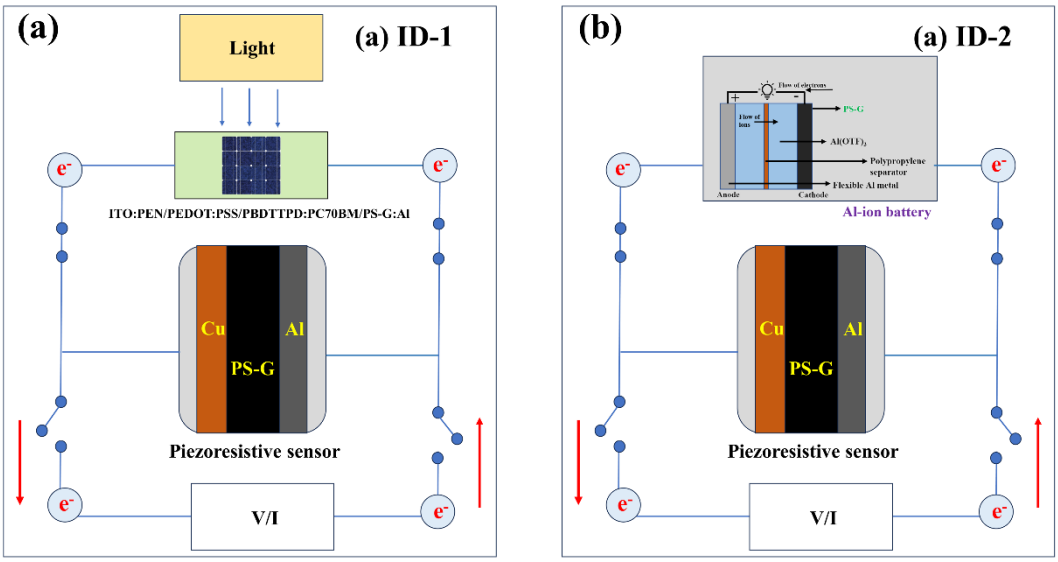

Fig. 9 Schematic diagram of (a) ID-1 (solar combined sensor) and (b) ID-2 (battery combined sensor).

4. Conclusion

It was demonstrated how sensors powered by batteries, flexible solar cells, and sustainable carbon electrodes could all work together. However, there is still room for improvement in terms of sensor performance. A flexible OPV without a metal top electrode with a PCE of 0.89% and an Al-carbon battery with a specific capacity of 148 mA hg^{-1} at 50 mAg^{-1} are being displayed in this work. To improve the setup of the integrated device, it is necessary to further investigate the battery's charge storage mechanism and the sensor's sensitive response. The

study as a whole presents a distinct perspective on the use of carbon produced from trash for self-powered applications in transdisciplinary sectors.

Supplementary Information: Supplementary.docx, Suppelementary.zip (Video Files)

Authors Contributions

BR conceptualized the work, fabricated the device, collected, and curated data, analyzed and wrote the discussion; VSR helped in fabrication of sensor, analyzed and interpreted the results; GWP helped in fabrication of solar cell and manuscript writing; YL helped in manuscript writing and editing; SR conceptualized the work, helped in manuscript writing and technical discussion; VC conceptualized the work, helped in manuscript writing, technical discussion and performed overall supervision

Acknowledgement

BR acknowledges A-STAR-SINGA (SING-2021-02-0819), offered by Agency for Science, Technology and Research (A*STAR) Singapore.

Conflict of Interest

No conflict of interest to disclose

Data availability statement

Data will be made available upon request

Ethical statement

This study has used human subjects for device testing with consent from the respective individual. The devices have been tested on BR (author) of the manuscript and the photographs has been used in the manuscript with the consent of the subject. All authors have agreed to the human machine interface testing and there are no ethical conflicts to disclose.

References

[1] J. DeAngelo, I. Azevedo, J. Bistline, L. Clarke, G. Luderer, E. Byers, S.J. Davis, Energy systems in scenarios at net-zero CO2 emissions, Nature Communications 2021 12:1 12 (2021) 1–10. https://doi.org/10.1038/s41467-021-26356-y.

[2] X.L. Shi, W.Y. Chen, T. Zhang, J. Zou, Z.G. Chen, Fiber-based thermoelectrics for solid, portable, and wearable electronics, Energy Environ Sci 14 (2021) 729–764. https://doi.org/10.1039/D0EE03520C.

[3] M. Kumar Malik, T. Kumar, V. Kumar, J. Singh, R. Kumar Singh, K. Saini, Sustainable, highly foldable, eco-friendly films from Mandua starch derivative, Sustainable Energy Technologies and Assessments 53 (2022) 102398. https://doi.org/10.1016/J.SETA.2022.102398.

[4] N. Kajiwara, H. Matsukami, G. Malarvannan, P. Chakraborty, A. Covaci, H. Takigami, Recycling plastics containing decabromodiphenyl ether into new consumer products including children's toys purchased in Japan and seventeen other countries, Chemosphere 289 (2022) 133179. https://doi.org/10.1016/J.CHEMOSPHERE.2021.133179.

[5] M. Aizudin, R. Goei, A.J. Ong, Y.Z. Tan, S.K. Lua, R.P. Pottammel, H. Geng, X.-L. Wu, A.L.Y. Tok, E.H. Ang, Sustainable development of graphitic carbon nanosheets from plastic wastes with efficient photothermal energy conversion for enhanced solar evaporation, J Mater Chem A Mater 10 (2022) 19612–19617. https://doi.org/10.1039/D2TA02092K.

[6] K. Fukuda, K. Yu, T. Someya, The Future of Flexible Organic Solar Cells, Adv Energy Mater 10 (2020) 2000765. https://doi.org/10.1002/AENM.202000765.

[7] Y. Sun, T. Liu, Y. Kan, K. Gao, B. Tang, Y. Li, Flexible Organic Solar Cells: Progress and Challenges, Small Science 1 (2021) 2100001. https://doi.org/10.1002/SMSC.202100001.

[8] F. Yang, Y. Huang, Y. Li, Y. Li, Large-area flexible organic solar cells, Npj Flexible Electronics 2021 5:1 5 (2021) 1–12. https://doi.org/10.1038/s41528-021-00128-6.

[9] Y. Sun, T. Liu, Y. Kan, K. Gao, B. Tang, Y. Li, Flexible Organic Solar Cells: Progress and Challenges, Small Science 1 (2021) 2100001. https://doi.org/10.1002/SMSC.202100001.

[10] J. Wan, X. Fan, Y. Li, P. Li, T. Zhang, K.N. Hui, H. Huang, K. Kang, L. Qian, High-Efficiency Flexible Organic Photovoltaics and Thermoelectricities Based on Thionyl Chloride Treated PEDOT:PSS Electrodes, Front Chem 9 (2022) 807538. https://doi.org/10.3389/FCHEM.2021.807538/BIBTEX.

[11] S.H. Kuan, Y. Ghorbani, S. Chieng, Narrowing the gap between local standards and global best practices in bauxite mining: A case study in Malaysia, Resources Policy 66 (2020) 101636. https://doi.org/10.1016/J.RESOURPOL.2020.101636.

[12] P. Wang, Z. Chen, Z. Ji, Y. Feng, J. Wang, J. Liu, M. Hu, H. Wang, W. Gan, Y. Huang, A flexible aqueous Al ion rechargeable full battery, Chemical Engineering Journal 373 (2019) 580–586. https://doi.org/10.1016/J.CEJ.2019.05.085.

[13] Z. Yu, S. Jiao, S. Li, X. Chen, W.L. Song, T. Teng, J. Tu, H. sen Chen, G. Zhang, D.N. Fang, Flexible Stable Solid-State Al-Ion Batteries, Adv Funct Mater 29 (2019) 1806799. https://doi.org/10.1002/ADFM.201806799.

[14] N. Sezer, M. Koç, A comprehensive review on the state-of-the-art of piezoelectric energy harvesting, Nano Energy 80 (2021) 105567. https://doi.org/10.1016/J.NANOEN.2020.105567.

[15] E.I. Shkolnikov, E.M. Novaev, S.A. Kochanova, A.S. Ilyukhin, D.E. Vervikishko, T.F. Yudina, I. v. Bratkov, L.M. Glukhov, Carbon materials as a cathode for aluminum-ion battery, Mater Today Proc 5 (2018) 26073–26077. https://doi.org/10.1016/J.MATPR.2018.08.032.

[16] G.A. Elia, K. v. Kravchyk, M. v. Kovalenko, J. Chacón, A. Holland, R.G.A. Wills, An overview and prospective on Al and Al-ion battery technologies, J Power Sources 481 (2021) 228870. https://doi.org/10.1016/J.JPOWSOUR.2020.228870.

[17] W. Xing, D. Du, T. Cai, X. Li, J. Zhou, Y. Chai, Q. Xue, Z. Yan, Carbon-encapsulated CoSe nanoparticles derived from metal-organic frameworks as advanced cathode material for Al-ion battery, J Power Sources 401 (2018) 6–12. https://doi.org/10.1016/J.JPOWSOUR.2018.08.079.

[18] M. Riede, D. Spoltore, K. Leo, Organic Solar Cells—The Path to Commercial Success, Adv Energy Mater 11 (2021) 2002653. https://doi.org/10.1002/AENM.202002653.

[19] F. Liu, L. Zhou, W. Liu, Z. Zhou, Q. Yue, W. Zheng, R. Sun, W. Liu, S. Xu, H. Fan, L. Feng, Y. Yi, W. Zhang, X. Zhu, Organic Solar Cells with 18% Efficiency Enabled by an Alloy Acceptor: A Two-in-One Strategy, Advanced Materials 33 (2021) 2100830. https://doi.org/10.1002/ADMA.202100830.

[20] C. Liu, C. Xiao, C. Xie, W. Li, Flexible organic solar cells: Materials, large-area fabrication techniques and potential applications, Nano Energy 89 (2021) 106399. https://doi.org/10.1016/J.NANOEN.2021.106399.

[21] L. Duan, A. Uddin, Progress in Stability of Organic Solar Cells, Advanced Science 7 (2020) 1903259. https://doi.org/10.1002/ADVS.201903259.

[22] Y. Tong, Z. Xiao, X. Du, C. Zuo, Y. Li, M. Lv, Y. Yuan, C. Yi, F. Hao, Y. Hua, T. Lei, Q. Lin, K. Sun, D. Zhao, C. Duan, X. Shao, W. Li, H.L. Yip, Z. Xiao, B. Zhang, Q. Bian, Y. Cheng, S. Liu, M. Cheng, Z. Jin, S. Yang, L. Ding, Progress of the key materials for organic solar cells, Science China Chemistry 2020 63:6 63 (2020) 758–765. https://doi.org/10.1007/S11426-020-9726-0.

[23] C. Dyer-Smith, I.A. Howard, C. Cabanetos, A. el Labban, P.M. Beaujuge, F. Laquai, Interplay between side chain pattern, polymer aggregation, and charge carrier dynamics in PBDTTPD:PCBM bulk-heterojunction solar cells, Adv Energy Mater 5 (2015). https://doi.org/10.1002/AENM.201401778.

[24] V. Chellappan, G.M. Ng, M.J. Tan, W.P. Goh, F. Zhu, Imbalanced charge mobility in oxygen treated polythiophene/fullerene based bulk heterojunction solar cells, Appl Phys Lett 95 (2009) 263305. https://doi.org/10.1063/1.3279135.

[25] K. Zhang, T.H. Lee, J.H. Cha, H.W. Jang, J.W. Choi, M. Mahmoudi, M. Shokouhimehr, Metal-organic framework-derived metal oxide nanoparticles@reduced graphene oxide composites as cathode materials for rechargeable aluminium-ion batteries, Scientific Reports 2019 9:1 9 (2019) 1–8. https://doi.org/10.1038/s41598-019-50156-6.

[26] H.A.A. Jamjoum, K. Umar, R. Adnan, M.R. Razali, M.N. Mohamad Ibrahim, Synthesis, Characterization, and Photocatalytic Activities of Graphene Oxide/metal Oxides

Nanocomposites: A Review, Front Chem 9 (2021) 789. https://doi.org/10.3389/FCHEM.2021.752276/BIBTEX.

[27] W. Luo, A.B. Kuzmenko, J. Qi, N. Zhang, W. Wu, M. Ren, X. Zhang, W. Cai, J. Xu, Nanoinfrared Characterization of Bilayer Graphene Conductivity under Dual-Gate Tuning, Nano Lett 21 (2021) 5151–5157. https://doi.org/10.1021/ACS.NANOLETT.1C01167/SUPPL_FILE/NL1C01167_SI_001.PDF.

[28] M. Sandhya, D. Ramasamy, K. Sudhakar, K. Kadirgama, M. Samykano, W.S.W. Harun, G. Najafi, M. Mofijur, M. Mazlan, A systematic review on graphene-based nanofluids application in renewable energy systems: Preparation, characterization, and thermophysical properties, Sustainable Energy Technologies and Assessments 44 (2021) 101058. https://doi.org/10.1016/J.SETA.2021.101058.

[29] S. Gong, D. Wu, Y. Li, M. Jin, T. Xiao, Y. Wang, Z. Xiao, Z. Zhu, Z. Li, Temperature-independent piezoresistive sensors based on carbon nanotube/polymer nanocomposite, Carbon N Y 137 (2018) 188–195. https://doi.org/10.1016/J.CARBON.2018.05.029.

[30] X. Zhang, D. Xiang, W. Zhu, Y. Zheng, E. Harkin-Jones, P. Wang, C. Zhao, H. Li, B. Wang, Y. Li, Flexible and high-performance piezoresistive strain sensors based on carbon nanoparticles@polyurethane sponges, Compos Sci Technol 200 (2020) 108437. https://doi.org/10.1016/J.COMPSCITECH.2020.108437.

[31] K.K. Kumar, R. Brindha, M. Nandhini, M. Selvam, K. Saminathan, K. Sakthipandi, Water-suspended graphene as electrolyte additive in zinc-air alkaline battery system, Ionics 2019 25:4 25 (2019) 1699–1706. https://doi.org/10.1007/S11581-019-02924-7.